

Controlled Surface Modification of ZnO Nanostructures with Amorphous TiO₂ for Photoelectrochemical Water Splitting

Alberto Gasparotto,* Chiara Maccato, Cinzia Sada, Giorgio Carraro, Dimitris I. Kondarides, Symeon Bebelis, Athanasia Petala, Andrea La Porta, Thomas Altantzis, and Davide Barreca

The utilization of solar radiation to trigger photoelectrochemical (PEC) water splitting has gained interest for sustainable energy production. In this study, attention is focused on the development of ZnO–TiO₂ nanocomposite photoanodes. The target systems are obtained by growing porous arrays of highly crystalline, elongated ZnO nanostructures on indium tin oxide (ITO) by chemical vapor deposition. Subsequently, the obtained nanodeposits are functionalized with TiO₂ via radio frequency-sputtering for different process durations, and subjected to final annealing in air. Characterization results demonstrate the successful formation of high purity composite systems in which the surface of ZnO nanostructures is decorated by ultra-small amounts of amorphous titania, whose content can be conveniently tailored as a function of deposition time. Photocurrent density measurements in sunlight-triggered water splitting highlight a remarkable performance enhancement with respect to single-phase zinc and titanium oxides, with up to a threefold photocurrent increase compared to bare ZnO. These results, mainly traced back to the formation of ZnO/TiO₂ heterojunctions yielding an improved photocarrier separation, show that the target nanocomposites are attractive photoanodes for efficient PEC water splitting.

1. Introduction

Photoelectrochemical (PEC) water splitting, harvesting sunlight to produce hydrogen from water, holds a significant promise for sustainable energy generation.^[1–4] Since the first demonstration of PEC water splitting over TiO₂ photoelectrodes in 1972, great efforts have been made to develop cost-effective semiconductor-based photoelectrode materials with improved catalytic activity and enhanced operational stability.^[5–7] Nevertheless, the limited process efficiency^[8–10] has continuously stimulated the search for novel strategies aimed at the size- and morphology-controlled design of oxide-based photoelectrode materials with improved performances. Various efforts have also been dedicated to their modification with dopants, quantum dots, plasmonic nanoparticles, electrocatalysts, or to the controlled fabrication of heterostructures with engineered interfacial properties.^[2,3,6,11–16]

In this context, ZnO, a largely abundant, low-cost, and non-toxic n-type semiconductor with a direct band gap of 3.3 eV, has emerged as an appealing photoanode material, since it combines suitable band energetics for water oxidation with high electron mobility (10–100 times larger than TiO₂).^[2,3,5,6,11,13,14,16,17] In addition, ZnO easily develops high surface area nanostructures that are desirable to maximize the contact area with the reaction medium, and typically feature high crystallinity and reduced grain boundary content, thus favoring charge transport phenomena.^[9,15,18,19] Nevertheless, these ZnO advantages are at least partially eclipsed by a poor catalytic activity, a limited stability in aqueous solutions, and a high recombination rate of photogenerated charge carriers.^[1,6,13,14] A valuable approach to circumvent these limitations involves the coupling of ZnO with TiO₂, thus developing composite materials featuring a synergistic combination of the single oxide properties. In fact, ZnO–TiO₂ systems offer a higher chemical reactivity and enhanced stability, along with the passivation of traps centers on ZnO surface responsible for charge recombination.^[4,17,18,20,21] In addition, due to a type-II band offset in which both the valence and conduction band edges of titania lie above those of ZnO, the formation of ZnO–TiO₂ heterojunctions yields a more efficient separation of photogenerated electrons and holes, disclosing attractive perspectives for PEC end-uses.^[5,10,16,21–26] Although


Prof. A. Gasparotto, Prof. C. Maccato, Dr. G. Carraro
Department of Chemical Sciences
Padova University and INSTM
35131 Padova, Italy
E-mail: alberto.gasparotto@unipd.it

Prof. C. Sada
Department of Physics and Astronomy
Padova University and INSTM
35131 Padova, Italy

Prof. D. I. Kondarides, Prof. S. Bebelis, Dr. A. Petala
Department of Chemical Engineering
University of Patras
26504 Patras, Greece

Dr. A. La Porta, Prof. T. Altantzis
EMAT
University of Antwerp
2020 Antwerpen, Belgium

Dr. D. Barreca
CNR-ICMATE and INSTM
Department of Chemical Sciences
Padova University
35131 Padova, Italy

 The ORCID identification number(s) for the author(s) of this article can be found under <https://doi.org/10.1002/adsu.201900046>.

DOI: 10.1002/adsu.201900046

ZnO–TiO₂ systems have been already investigated for such applications,^[7,8,21,24,27–29] most of the related works have been focused on composite materials containing a comparable amount of the two oxides and sometimes suffering from a limited control over particle size, interfacial quality, and material morphology. In a different way, the controlled surface modification of “supported” ZnO-based nanostructures through the introduction of low TiO₂ amounts in the form of highly dispersed nanoparticles or ultrathin (<5 nm) layers has been comparatively less studied,^[9,30,31] although such a strategy appears very promising to attain improved functional performances. In fact, whereas a thick TiO₂ overlayer ensures an efficient photocorrosion protection of the underlying ZnO, it can inhibit electron transfer from the electrolyte to the substrate.^[32] Conversely, an ultrathin titania overlayer can yield an optimal ZnO corrosion resistance without suppressing water oxidation performances, avoiding, at the same time, a detrimental ZnO porosity reduction.^[4,9,16]

In the above context, TiO₂ has gained a renewed interest for photoelectrochemical applications especially in its amorphous form (a-TiO₂). The latter shows in fact optical properties similar to crystalline TiO₂,^[33,34] yet coupled to a high structural flexibility and an improved electrical conductivity.^[3,23,35–41] a-TiO₂ is also preferable to polycrystalline TiO₂ since crystal boundaries are always vulnerable sites originating detrimental corrosion phenomena. In a different way, amorphous TiO₂ enables to circumvent this drawback and generally yields superior performances as passivation layer, suppressing carrier recombination and resulting in an enhanced system stability.^[16] To date, surface decoration with amorphous TiO₂ has indeed been reported to successfully stabilize Si, GaAs, and GaP photoanodes for water oxidation in alkaline media,^[40] to promote hydrogen evolution from water over CdSe nanocrystals^[41] and to enhance PEC performances of ZnO nanorod arrays by passivating surface trap states.^[25]

On this basis, the present work is focused on the ad hoc surface decoration of ZnO nanostructured electrodes with low amounts of a-TiO₂ by means of a hybrid vapor phase route, involving the growth of ZnO nanostructures by chemical vapor deposition (CVD) and their subsequent functionalization with TiO₂ by radio frequency (RF)-sputtering. To the best of our knowledge, no previous reports on the preparation of ZnO–TiO₂ nanomaterials by the above mentioned route are available in the literature to date. The resulting materials were characterized in detail in their composition, structure/morphology, and optical properties, and finally tested in PEC water splitting triggered by simulated solar light. It was found that ZnO functionalization with an optimal TiO₂ amount yields a nearly threefold increase in photocurrent values compared to bare ZnO. The impact of these results and their interplay with the preparative conditions are presented and critically discussed below.

2. Results and Discussion

Basing on a recent work on the CVD growth of bare ZnO materials,^[42] we focus herein on the preparation of ZnO–TiO₂ systems and, in particular, on the tailored modification of zinc oxide

surface by very low titania amounts. Specifically, in the present study, ZnO nanomaterials were grown on indium tin oxide (ITO) substrates under optimized conditions, and TiO₂ was subsequently deposited onto ZnO via RF-sputtering from a titanium target and subsequent air annealing. Two different sputtering times, namely 2 and 4 h, were used to fabricate TiO₂-decorated ZnO-based systems with a different TiO₂ loading (hereafter indicated as ZnO–TiO₂(2 h) and ZnO–TiO₂(4 h), respectively).

The chemico-physical properties and PEC performances of the obtained composites were investigated by means of a multitechnique characterization approach. To preliminarily ascertain the system purity and surface composition, X-ray photoelectron spectroscopy (XPS) analyses were carried out. **Figure 1a** displays the wide scan XPS spectra of ZnO and ZnO–TiO₂(4 h) specimens, as representative examples. The former sample revealed the expected Zn and O photopeaks,^[42–44] along with the presence of carbon species arising from atmospheric contamination (<10 atomic percentage (at%)). In addition to these elements, titanium presence could be also evidenced for specimen ZnO–TiO₂(4 h). A detailed photoelectron peak analysis (see Figure S1a–c, Supporting Information) revealed the copresence of ZnO and TiO₂, and enabled to discard the formation of Zn–O–Ti ternary phases, consistently with electron microscopy results. The titanium surface molar fraction X_{Ti} was 10.0% and 18.0% for ZnO–TiO₂(2 h) and ZnO–TiO₂(4 h), respectively. To investigate the in-depth composition of such specimens, secondary ion mass spectrometry (SIMS) analyses were also carried out (Figure 1b,c). The mean C concentration was estimated to be lower than 125 ppm, highlighting the purity of the obtained nanomaterials. O and Zn ionic yields

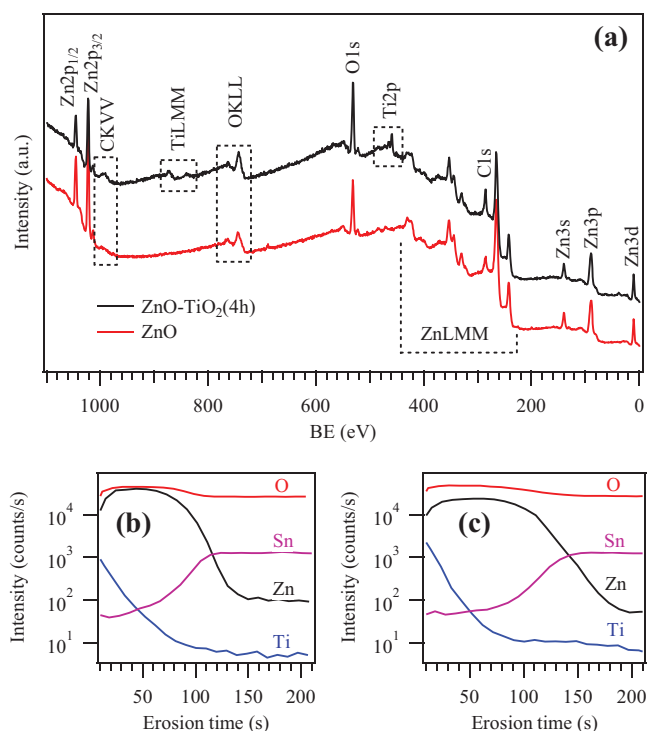


Figure 1. a) XPS survey spectra of bare ZnO and ZnO–TiO₂(4 h) samples. SIMS depth profiles for specimens b) ZnO–TiO₂(2 h) and c) ZnO–TiO₂(4 h).

remained almost constant throughout the specimen depth, consistently with the uniform presence of zinc oxide. In a different way, despite the fact that the outermost layers were Ti-rich, titanium signal was well detectable even in the inner deposit regions. This result, due to the efficient infiltration of sputtered titanium species into the ZnO porous structure, suggested the occurrence of an intimate ZnO/TiO₂ contact throughout the sampled depth, a crucial issue to benefit from their mutual electronic interplay, positively boosting the composite material photoresponse (see below). The apparent tailing of tin signals from the substrate into the ZnO deposits was mainly ascribed to the high deposit/substrate interfacial roughness. The relative intensities of Ti and Zn ionic yields in the two samples suggested a higher TiO₂ amount for specimen ZnO–TiO₂(4 h), in line with the longer sputtering time adopted in this latter case.

The system morphology was analyzed by the combined use of field emission-scanning electron microscopy (FE-SEM) and atomic force microscopy (AFM). FE-SEM images (Figure S2a,b, Supporting Information) revealed the formation of uniformly interconnected nanoaggregates assembled into porous arrays, with voids extending deep into the system structure. For bare ZnO, both the average nanoaggregate lateral size and overall deposit thickness were estimated to be ≈200 nm. Functionalization with TiO₂ resulted in more rounded and slightly larger (≈250 nm) surface features, but did not yield drastic modification of the pristine ZnO nanorganization, thanks to the relatively mild conditions adopted during RF-sputtering. Coherently with these results, AFM images displayed a uniform topography characterized by arrays of elongated nanostructures (Figure S2c,d, Supporting Information). Images recorded on different regions enabled to confirm the specimen homogeneity. Overall, such a morphology can be deemed to be favorable for PEC applications, since the low aggregate lateral dimensions can minimize the diffusion distance of holes to the photoanode surface, whereas the relatively large axial dimensions simultaneously enable an enhanced light absorption and a directional electron transport toward the ITO substrate.^[2,5–7,23,27,45]

Material structure was preliminarily characterized by glancing incidence X-ray diffraction (GIXRD) analysis. The recorded patterns (Figure S3, Supporting Information) for bare and TiO₂-functionalized ZnO systems were almost identical and, apart from peaks due to the ITO substrate, revealed only reflections attributable to the (002), (101), and (102) planes of hexagonal ZnO (wurtzite) at 34.5°, 36.3°, and 47.6°, respectively.^[46] The absence of intensity variations and angular shifts indicated that the original ZnO structure was preserved, ruling out the formation of mixed oxide phases under the adopted processing conditions, in line with XPS characterization (see above). No signals related to TiO₂ polymorphs could be unambiguously observed, despite a glancing incidence configuration was used to maximize surface sensitivity. To investigate in more detail the nanoscale structure of the developed nanocomposite systems, advanced high angle annular dark-field scanning transmission electron microscopy (HAADF-STEM) and energy dispersive X-ray spectroscopy (EDXS) analyses were carried out. **Figure 2a,b** displays an HAADF-STEM overview cross-sectional image and an EDXS chemical map for sample ZnO–TiO₂(2 h). The obtained results confirmed that the

polycrystalline ZnO deposit was composed of elongated nanostructures (average lateral size ≈ 100 nm) grown perpendicularly to the ITO substrate surface, forming a porous deposit. Although TiO₂ appeared to be mainly concentrated on the top of ZnO nanostructures (see the pink region in Figure 2b), consistently with SIMS results (compare Figure 1b,c), a closer look at the elemental distribution revealed that titania was dispersed even in the inner sample regions, an important issue to proficiently exploit cooperative interfacial effects between the two oxides.^[43,47,48]

To this aim, Figure 2c shows a representative HAADF-STEM image of an individual ZnO grain. The corresponding EDXS maps and the Fourier transform (FT) pattern are displayed in Figure 2d–f. The obtained results clearly revealed that the ZnO structure in the central region of Figure 2c was uniformly covered by a thin titania overlayer, whose average thickness was comprised between 1 and 2 nm (Figure 2e). From the FT pattern it is clear that the ZnO deposit was highly crystalline and possessed the zincite structure^[46] (Figure 2f), whereas titania was present in an amorphous phase. This result is in line with the absence of titania-related reflections in the obtained GIXRD patterns (see above).

An HAADF-STEM overview image of sample ZnO–TiO₂(4 h) is presented in Figure S4a of the Supporting Information. As can be observed, the ZnO nanodeposit displayed very similar features to those already discussed for specimen ZnO–TiO₂(2 h). As far as the elemental composition is concerned, EDXS maps shown in Figure S4b of the Supporting Information suggest that ZnO particles are covered by a TiO₂ overlayer thicker than sample ZnO–TiO₂(2 h). This feature, arising from the use of a longer sputtering time, was indeed supported by high-resolution HAADF-STEM images, revealing the presence of highly crystalline ZnO structures conformally covered by an amorphous TiO₂ overlayer (Figure S4c–f, Supporting Information). In particular, a statistical analysis on diverse sample regions (compare Figure S4c–e with Figure S5a–f, Supporting Information) confirmed the obtainment of a conformal titania layer with an average thickness of 3–4 nm, a value approximately two times higher than that of the previous specimen. Although such an investigation also supported the amorphous nature of titania, the presence of residual amounts of crystalline TiO₂ cannot be completely discarded.

The optical properties of bare and TiO₂-decorated ZnO-based systems were investigated by optical absorption spectroscopy (**Figure 3**). As can be observed, titania introduction did not appreciably modify the spectrum of pure ZnO, neither in terms of onset position, nor in terms of absorption intensity (Figure 3a). Irrespective of TiO₂ presence, the samples displayed a high transparency in the visible region and a sharp absorption edge for $\lambda \leq 370$ nm, related to the characteristic ZnO interband transitions.^[47,49] Accordingly, the trends of the absorption coefficient versus photon energy shown in Figure 3b,c revealed very similar profiles, yielding optical band gap values of ≈3.25 eV, consistently with literature data for ZnO systems.^[22,27,43,47] Such results confirm that no significant zinc oxide doping occurred and that the single-phase oxides maintained their chemical identity, a feature traced back to the mild processing conditions of the adopted synthetic approach.^[43,47]

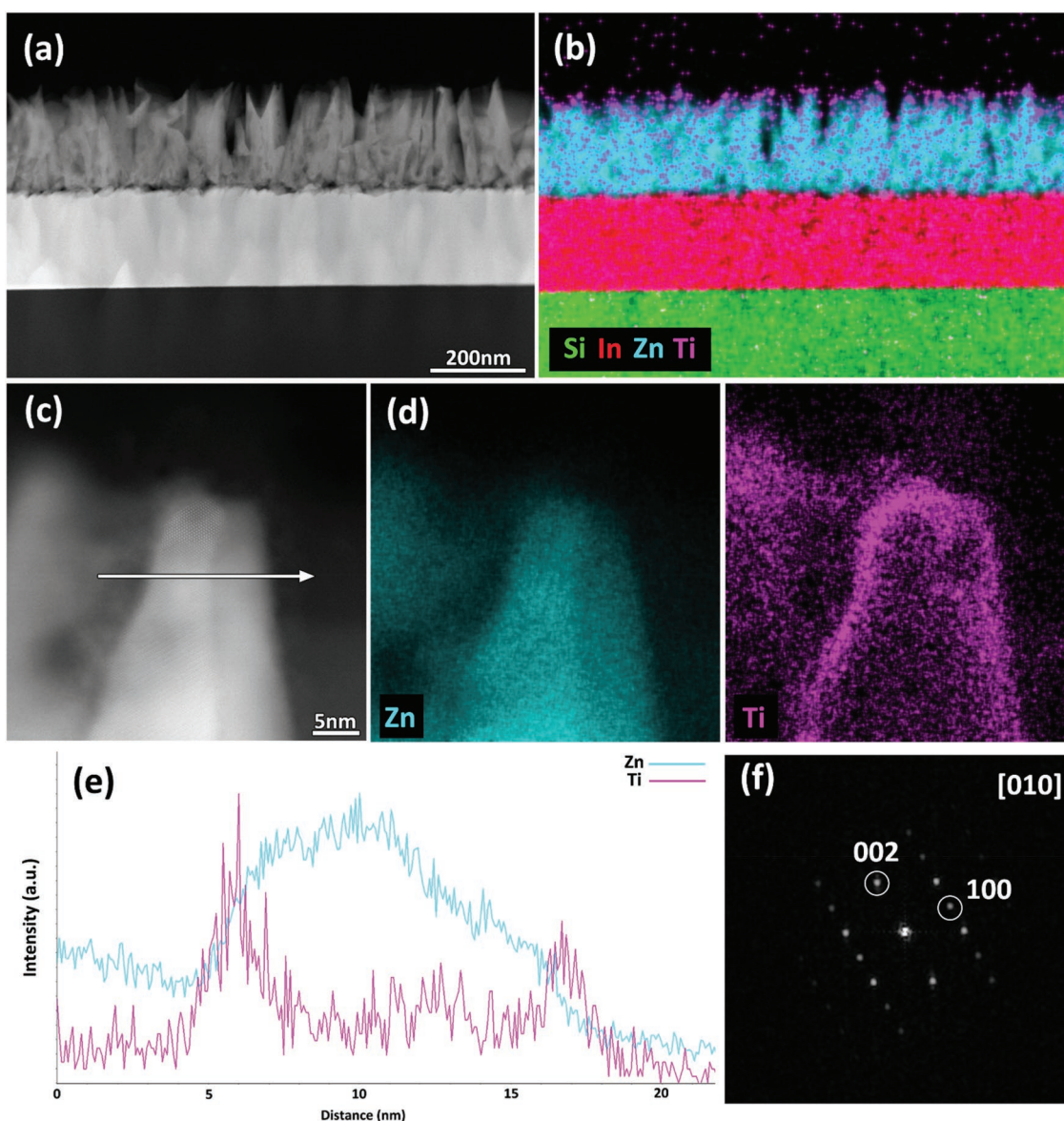


Figure 2. a) Cross-sectional HAADF-STEM image of sample ZnO–TiO₂(2 h). b) EDXS elemental maps for Si, In, Zn, and Ti, acquired from the same region. c) HAADF-STEM image of a TiO₂-decorated ZnO crystal oriented along the [010] zone axis, and d) corresponding EDXS maps for Zn and Ti. e) EDXS line-scans along the white line in (c). f) FT pattern from the crystal at the center of panel (c).

Photoelectrochemical performances of ZnO and ZnO–TiO₂ systems were investigated in 0.1 M NaOH by measuring the current/voltage characteristics in dark and under irradiation. The obtained current density versus applied potential curves, corresponding to the anodic sweep part of the cyclic voltammograms, are presented in Figure S6a–d, Supporting Information), whereas **Figure 4a** displays the polarization curves for the four tested samples under irradiation. Moreover, to facilitate comparison, **Table 1** lists the measured values of the open-circuit voltage (V_{OC}), as well as the photocurrent density at 0.25 V versus Ag/AgCl.

The data in Figure S6a–d (Supporting Information) and Table 1 show that V_{OC} decreases under illumination and shifts toward more negative values for ZnO–TiO₂ composites compared to the single phase oxides. This phenomenon implies a

shift of the flat band potential toward more negative values,^[29] and provides evidence that a-TiO₂ promotes the oxygen evolution reaction, likely due to the presence of unsaturated defect sites on its surface.^[35–37,39]

The bare TiO₂ sample shows a negligible activity, since similar curves were obtained both in the dark and under illumination (Figure S6a, Supporting Information). This behavior can be associated to the modest catalytic activity of a-TiO₂^[33,41,50,51] and the very small deposited material amount.

At variance with TiO₂, bare ZnO gives appreciable photocurrent densities for applied potentials higher than –0.5 V versus Ag/AgCl (Figure S6b, Supporting Information; Figure 4a) and, in particular, produces 0.36 mA cm^{–2} at 0.25 V versus Ag/AgCl (see Table 1). Notably, this value compares favorably with, or even outperforms, literature data for pristine ZnO

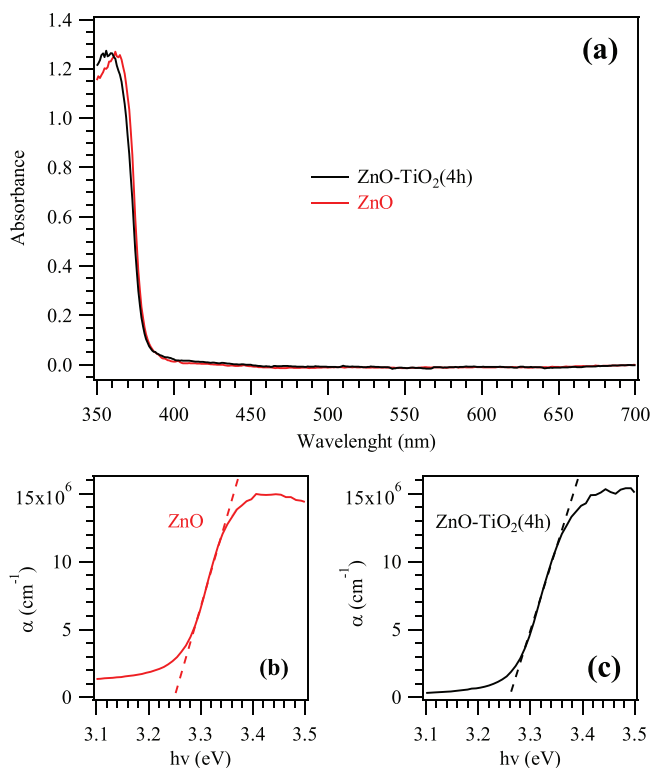


Figure 3. a) Optical absorption spectra and b,c) absorption coefficient versus photon energy plots for bare ZnO and ZnO–TiO₂(4 h) samples.

photoanodes.^[3,11,13,27,43,45,52] The promising performances of the present ZnO systems can be attributed to a concurrence of different effects, namely, the high ZnO crystallinity, the reduced content of grain boundaries and defects, the high porosity, and the good interfacial contact with the ITO substrate.^[2,19,45]

Interestingly, TiO₂ deposition onto ZnO yielded a remarkable performance improvement compared to pure ZnO (Figure S6c,d, Supporting Information; Figure 4a) as well as a steeper photocurrent increase with the applied potential, indicating the occurrence of beneficial synergistic effects between the two oxides. As a figure of merit, ZnO–TiO₂(2 h) and ZnO–TiO₂(4 h) exhibited photocurrent densities at 0.25 V versus Ag/AgCl of 0.93 and 0.77 mA cm⁻², respectively (Table 1). These results are comparable or even better than those reported for other TiO₂-functionalized ZnO-based photoanodes.^[9,27,29,31,53]

As shown in Figure 4a, at 0.85 V versus Ag/AgCl, which marks the end of the saturation photocurrent region for bare ZnO, the photocurrent density for ZnO–TiO₂(4 h) was slightly higher than that for ZnO–TiO₂(2 h), with a nearly threefold enhancement in comparison to pure ZnO. The increased photocurrent densities obtained for TiO₂-functionalized ZnO indicated an improved electron–hole separation efficiency compared to the pristine zinc oxide.^[29] This conclusion is also supported by the absence of photocurrent saturation at higher positive potentials upon illumination.^[31,53,54] The slightly lower (by ≈40 mV) onset potential for ZnO–TiO₂(4 h) may reflect a reduced surface recombination, as the latter typically dominates bulk recombination at lower bias. At higher applied potentials,

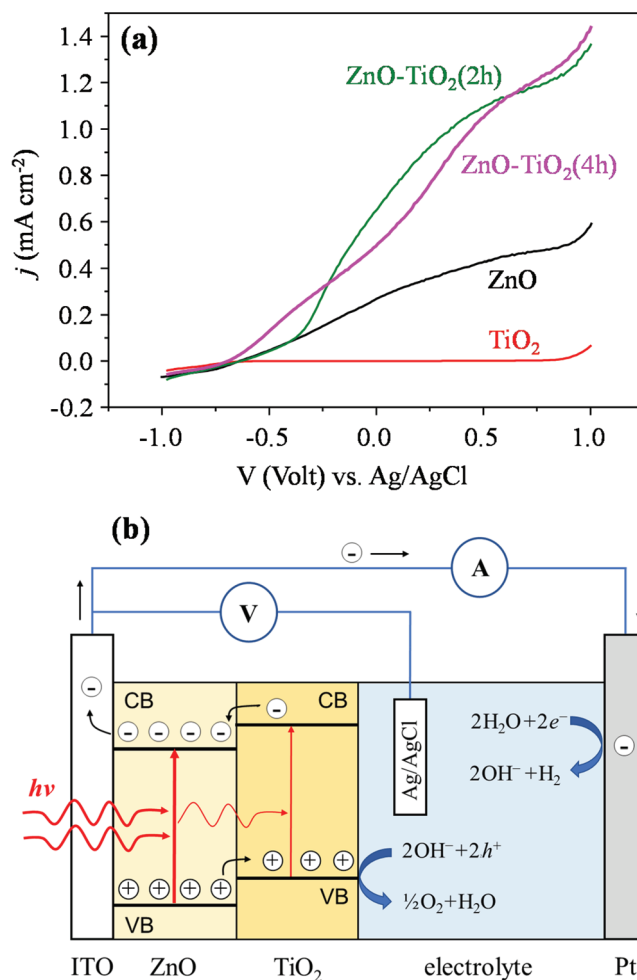


Figure 4. a) Synoptic overview of photocurrent density versus applied potential curves for single phase and composite electrode materials. b) Simplified diagram showing the energy band structure (CB = conduction band edge; VB = valence band edge) at the ZnO/TiO₂ heterojunction and the main phenomena and reactions occurring in the three-electrode PEC cell.

ZnO–TiO₂(2 h) exhibited better performances than ZnO–TiO₂(4 h), due to an enhanced recombination suppression, as described below. It may be also noted that, although the formation of a thin α -TiO₂ shell completely covering ZnO minimizes the pinhole density, it may not allow efficient conduction of photogenerated holes thereby decreasing system efficiency.^[40]

Table 1. Open-circuit voltages and photocurrent density values for the target materials.

Sample	Open-circuit voltage (V _{oc}) [V] (vs Ag/AgCl)		Photocurrent density (<i>j</i> , mA cm ⁻²) at 0.25 V (vs Ag/AgCl)
	Dark	Light	
TiO ₂	-0.03	-0.38	0.00
ZnO	-0.13	-0.60	0.36
ZnO–TiO ₂ (2 h)	-0.13	-0.65	0.93
ZnO–TiO ₂ (4 h)	-0.18	-0.70	0.77

The combined data analysis enables to conclude that the higher photocurrents produced by the nanocomposite photoanodes are directly related to a mutual electronic interplay at the interfaces between ZnO and TiO₂. In this regard, the overall process taking place on the TiO₂-decorated ZnO photoanode can be better understood basing on the simplified diagram shown in Figure 4b, which displays the electronic effects resulting from the ZnO/TiO₂ heterojunction.

The process is initiated by absorption of ultraband gap photons from the active material. Due to the photoanode configuration (back side illumination) and the much higher ZnO amount compared to a-TiO₂, this event mainly takes place into the former oxide and involves the generation of e⁻/h⁺ pairs in the ZnO bulk. A portion of the incident photons may also reach and photoexcite the overlying a-TiO₂, resulting in the generation of additional charge carriers. Due to the relative positions of VB and CB edges of the two oxides,^[10,16,26,29,31,53] photogenerated electrons move toward ZnO, whereas photogenerated holes flow toward TiO₂. This process is favored by the intimate interfacial contact between a-TiO₂ and ZnO, demonstrated by the above discussed characterization results. As a consequence, charge carriers are spatially isolated, and their recombination rate is effectively suppressed, leading to prolonged electron/hole lifetimes. The underlying ZnO, which is characterized by high electron mobility,^[1,21,43] provides a preferential path for electron transfer to the ITO substrate and, subsequently, toward the Pt counter electrode, where water reduction to hydrogen takes place (Figure 4b). On the other hand, VB holes accumulated in the a-TiO₂ layer move toward the interface with the electrolyte, where they trigger oxidation processes leading to O₂ evolution. In addition, the above mentioned surface a-TiO₂ defects provide active sites for an efficient water adsorption and subsequent oxidation.^[3,33,41]

The transfer of photogenerated holes to a-TiO₂ and their consumption in water oxidation is also expected to suppress ZnO photocorrosion.^[25,40,55] Nevertheless, if the TiO₂ overlayer is too thick, the hole transfer to the electrolyte is hindered due to the relatively short hole diffusion length, as well as to the possible occurrence of trap states, resulting in a detrimental decrease of the process efficiency.^[10] As a matter of fact, due to the modest conductivity of the titania overlayer, its thickness needs to be carefully tailored.^[16]

Overall, the combination of the above effects yielded, for sample ZnO–TiO₂(2 h), photocurrent density values ≈2.5 times higher than those for bare ZnO, at 0.85 V versus Ag/AgCl. It is worth highlighting that this goal can be achieved thanks to ZnO decoration by a-TiO₂, provided that the amount and thickness of the latter is carefully controlled. Under such conditions, the functionalization of ZnO with a-TiO₂ might be a valid alternative to toxic and/or expensive materials (e.g., Au, Ag, IrO_x, RuO_x) typically used as cocatalysts or plasmonic nanoparticles for PEC and related applications.^[52,56,57]

3. Conclusions

In this work, ZnO–TiO₂ nanocomposites were fabricated by a hybrid vapor-phase approach, consisting in the initial CVD of ZnO nanosystems on ITO substrates, followed by the introduc-

tion of TiO₂ by RF-sputtering and final thermal treatment in air. The results obtained by a multitechnique characterization highlight the successful preparation of high purity nanomaterials, characterized by a controlled surface decoration of ZnO-based nanostructures by amorphous TiO₂ overlayers with an intimate contact between single-phase oxides. Interestingly, both the overall TiO₂ content and its thickness could be proficiently tailored by the sole variations of the sputtering time. These features had a very favorable impact on the system functional performance in photoelectrochemical water splitting under simulated sunlight, which yielded, under optimized conditions, a photocurrent density of ≈0.9 mA cm⁻² at 0.25 V versus Ag/AgCl and a downward onset potential shift (up to 40 mV). The appreciable ZnO–TiO₂ photoactivity amplification with respect to the pristine ZnO was mainly related to the efficient formation of ZnO–TiO₂ heterojunctions, responsible, in turn, for a suppressed recombination of photoproduced charge carriers. These effects could be maximized by a proper control of the TiO₂ overlayer thickness through the corresponding sputtering time.

Overall, the reported results highlight that the developed preparative strategy yields a very fine control over TiO₂ dispersion and the resulting ZnO–TiO₂ material features, paving the way to future mastering of the system characteristics toward development of more efficient photoanodes for water splitting. Furthermore, the potential of the synthetic approach proposed herein can be exploited for the controlled modification of a wide range of materials, paving the way to the implementation of light-activated functional systems with surface engineered properties. Future research efforts will be devoted to investigating the energy band structure of the developed ZnO–TiO₂ systems, as well as their long-term stability upon prolonged utilization, in view of their possible applications under real-world conditions.

4. Experimental Section

Synthesis: The growth of the target materials was carried out on suitably precleaned 1 × 2 cm² ITO-coated borosilicate glass slides (Präzisions Glas & Optik GmbH, CEC010B, 10 Ω sq⁻¹; ITO thickness ≈ 200 nm). Prior to sample preparation, a substrate region of 0.5 × 1 cm² was masked from deposition to make electrical contacts for the ultimate PEC tests.

ZnO deposits were synthesized at 350 °C by CVD using a custom-built hot-wall apparatus.^[58] Zn(hfa)₂TMEDA (hfa = 1,1,1,5,5,5-hexafluoro-2,4-pentanedionate; TMEDA = N,N,N',N'-tetramethylethylenediamine) was used as precursor, vaporized at 80 °C, and transported into the reaction chamber by electronic grade N₂ (flow rate = 100 standard cubic centimeters per minute (sccm)). An auxiliary electronic grade oxygen flow (rate = 30 sccm) was introduced separately into the reaction chamber after passing through a water reservoir maintained at 30 °C. The total pressure was set to 3.0 mbar, and the process duration was fixed to 2 h.^[42]

For the preparation of ZnO–TiO₂ systems, the above ZnO matrices were mounted on the ground electrode of an RF-sputtering reactor (ν = 13.56 MHz).^[47] Sputtering was performed using a titanium target (Alfa Aesar, purity = 99.95%) and electronic grade Ar plasmas (Ar flow rate = 10 sccm; total pressure = 0.3 mbar; RF-power = 20 W; interelectrode distance = 5 cm). The growth temperature was fixed at 60 °C, while the process duration was changed from 2 to 4 h to tailor the overall titania loading in the resulting systems. A bare TiO₂ sample,

prepared with a sputtering time of 4 h and using the conditions given above, was also synthesized on ITO for comparison purposes. All specimens were finally annealed in air ex situ at 350 °C for 1 h using a Carbolite HST 12/200 tubular furnace.

Characterization: XPS analyses were carried out on a Perkin-Elmer Φ 5600ci spectrometer, using a non-monochromatized Mg K α excitation source ($h\nu = 1253.6$ eV). The reported binding energies (BEs) were corrected for charging phenomena by assigning a BE of 284.8 eV to the C1s line of adventitious carbon.^[42,43] After a Shirley-type background subtraction, at% values were obtained using Φ V5.4A sensitivity factors. The titanium surface molar fraction was defined as $X_{Ti} = \{[(Ti \text{ at}\%) / \{(Ti \text{ at}\%) + (Zn \text{ at}\%)\}]\} \times 100$.

SIMS analyses were carried out on an IMS 4f mass spectrometer (Cameca), using a Cs⁺ primary ion beam (voltage = 14.5 keV; current = 30 nA, stability = 0.3%) and negative secondary ion detection, adopting an electron gun for charge compensation. Measurements were performed rastering over a 175 × 175 μm^2 area and collecting negative secondary ion signals from a 7 × 7 μm^2 region. Beam-blanking mode and high mass resolution configurations were adopted.

FE-SEM analyses were run on a Zeiss SUPRA 40 VP instrument, using a primary electron beam voltage of 20.0 kV. The ImageJ software (<http://imagej.nih.gov/ij/>, accessed: July 2018) was used to evaluate the average particle size and deposit thickness.

AFM images were collected on an NT-MDT SPM solver P47H-PRO instrument, operating in semicontact mode and in air. RMS roughness values were obtained from 3 × 3 μm^2 images after background subtraction.

GIXRD patterns were collected at an incidence angle of 1.0° by a Bruker D8 Advance instrument equipped with a Göbel mirror, using a CuK α X-ray source.

Samples for cross-sectional STEM observations were prepared by mechanical polishing, using an Allied Multiprep System with diamond-lapping films, down to a thickness of ≈ 20 μm , followed by Ar⁺ ion milling by using a Leica EM RES102 apparatus (acceleration voltages up to 4 kV; incident beam angles 6°–11°). Low and high-magnification HAADF-STEM images, as well as EDXS elemental maps, were acquired using an aberration corrected cubed FEI Titan electron microscope operated at 300 kV, equipped with the ChemiSTEM system.^[59] HAADF-STEM imaging was carried out using probe convergence and detector inner collection semiangles of 21 and 55 mrad, respectively.

Optical absorption spectra were collected on quartz-deposited samples in transmission mode at normal incidence with a Cary 5 spectrophotometer. In all cases, the substrate contribution was subtracted. Band gap values were estimated by fitting the linear portion of the absorption coefficient versus photon energy curves to zero absorption.

The experimental setup used for PEC measurements consisted of a solar light-simulating source (Xe Arc Lamp, Osram 300 W), the photoreactor, a potentiostat/galvanostat (PGSTAT 128N, Metrohm Autolab), and a gas chromatograph (Varian CP3800) connected on-line to the reactor exit. Experiments were conducted at room temperature under flowing Ar, employing a three-electrode PEC cell configuration and aqueous NaOH 0.1 M as electrolyte solution. More details are provided in the Supporting Information.

Supporting Information

Supporting Information is available from the Wiley Online Library or from the author.

Acknowledgements

This work was financially supported by Padova University DOR 2016–2019, P-DiSC #03BIRD2016-UNIPD, and #03BIRD2018-UNIPD projects and ACTION post-doc fellowship. A.G. acknowledges AMGA

Foundation and INSTM Consortium. T.A. acknowledges a postdoctoral grant from the Research Foundation Flanders (FWO, Belgium). Thanks are also due to Dr. Sebastiano Pianta (Department of Chemical Sciences, Padova University, Italy) for experimental assistance.

Conflict of Interest

The authors declare no conflict of interest.

Keywords

heterojunctions, photoelectrochemistry, TiO₂, water splitting, ZnO

Received: April 5, 2019

Revised: May 3, 2019

Published online:

- [1] A. U. Pawar, C. W. Kim, M. J. Kang, Y. S. Kang, *Nano Energy* **2016**, 20, 156.
- [2] B. Zhang, Z. Wang, B. Huang, X. Zhang, X. Qin, H. Li, Y. Dai, Y. Li, *Chem. Mater.* **2016**, 28, 6613.
- [3] Y. Mao, Y. Cheng, J. Wang, H. Yang, M. Li, J. Chen, M. Chao, Y. Tong, E. Liang, *New J. Chem.* **2016**, 40, 107.
- [4] R. Liu, Z. Zheng, J. Spurgeon, X. Yang, *Energy Environ. Sci.* **2014**, 7, 2504.
- [5] S. Cho, J.-W. Jang, K.-H. Lee, J. S. Lee, *APL Mater.* **2014**, 2, 010703.
- [6] C. Jiang, S. J. A. Moniz, M. Khraisheh, J. Tang, *Chem. - Eur. J.* **2014**, 20, 12954.
- [7] K. Pan, Y. Dong, W. Zhou, Q. Pan, Y. Xie, T. Xie, G. Tian, G. Wang, *ACS Appl. Mater. Interfaces* **2013**, 5, 8314.
- [8] D. Chen, H. Zhang, S. Hu, J. Li, *J. Phys. Chem. C* **2008**, 112, 117.
- [9] M. Liu, C.-Y. Nam, C. T. Black, J. Kamcev, L. Zhang, *J. Phys. Chem. C* **2013**, 117, 13396.
- [10] A. Ghobadi, T. G. U. Ghobadi, F. Karadas, E. Ozbay, *Sci. Rep.* **2018**, 8, 16322.
- [11] S. Xie, W. Wei, S. Huang, M. Li, P. Fang, X. Lu, Y. Tong, *J. Power Sources* **2015**, 297, 9.
- [12] E. M. P. Steinmiller, K.-S. Choi, *Proc. Natl. Acad. Sci. USA* **2009**, 106, 20633.
- [13] Y. Liu, X. Yan, Z. Kang, Y. Li, Y. Shen, Y. Sun, L. Wang, Y. Zhang, *Sci. Rep.* **2016**, 6, 29907.
- [14] S. G. Kumar, K. S. R. K. Rao, *RSC Adv.* **2015**, 5, 3306.
- [15] Z. Kang, X. Yan, Y. Wang, Z. Bai, Y. Liu, Z. Zhang, P. Lin, X. Zhang, H. Yuan, X. Zhang, Y. Zhang, *Sci. Rep.* **2015**, 5, 7882.
- [16] Z. Kang, H. Si, S. Zhang, J. Wu, Y. Sun, Q. Liao, Z. Zhang, Y. Zhang, *Adv. Funct. Mater.* **2019**, 29, 1808032.
- [17] C. Justin Raj, S. N. Karthick, A. Dennyson Savariraj, K. V. Hemalatha, S.-K. Park, H.-J. Kim, K. Prabakar, *J. Alloys Compd.* **2012**, 537, 159.
- [18] P. Labouchere, A. K. Chandiran, T. Moehl, H. Harms, S. Chavhan, R. Tena-Zaera, M. K. Nazeeruddin, M. Graetzel, N. Tetreault, *Adv. Energy Mater.* **2014**, 4, 1400217.
- [19] M. Law, L. E. Greene, A. Radenovic, T. Kuykendall, J. Liphardt, P. Yang, *J. Phys. Chem. B* **2006**, 110, 22652.
- [20] L. Wang, D. Yan, D. W. Shaffer, X. Ye, B. H. Layne, J. J. Concepcion, M. Liu, C.-Y. Nam, *Chem. Mater.* **2018**, 30, 324.
- [21] M. M. Momeni, Y. Chayeb, *J. Appl. Electrochem.* **2015**, 45, 557.
- [22] N. Todorova, T. Giannakopoulou, K. Pomoni, J. Yu, T. Vaimakis, C. Trapalis, *Catal. Today* **2015**, 252, 41.
- [23] H. Y. Yang, S. F. Yu, S. P. Lau, X. Zhang, D. D. Sun, G. Jun, *Small* **2009**, 5, 2260.

- [24] P. G. Ramos, E. Flores, L. A. Sánchez, R. J. Candal, M. Hojamberdiev, W. Estrada, J. Rodriguez, *Appl. Surf. Sci.* **2017**, *426*, 844.
- [25] D. Guo, J. Wang, C. Cui, P. Li, X. Zhong, F. Wang, S. Yuan, K. Zhang, Y. Zhou, *Sol. Energy* **2013**, *95*, 237.
- [26] N. A. Abd Samad, C. W. Lai, K. S. Lau, S. B. Abd Hamid, *Materials* **2016**, *9*, 937.
- [27] S. Hernández, V. Cauda, D. Hidalgo, V. Fariás Rivera, D. Manfredi, A. Chiodoni, F. C. Pirri, *J. Alloys Compd.* **2014**, *615*, S530.
- [28] F. Xu, J. Mei, X. Li, Y. Sun, D. Wu, Z. Gao, Q. Zhang, K. Jiang, *J. Nanopart. Res.* **2017**, *19*, 297.
- [29] S. Hernández, V. Cauda, A. Chiodoni, S. Dallorto, A. Sacco, D. Hidalgo, E. Celasco, C. F. Pirri, *ACS Appl. Mater. Interfaces* **2014**, *6*, 12153.
- [30] K. Appavoo, M. Liu, C. T. Black, M. Y. Sfeir, *Nano Lett.* **2015**, *15*, 1076.
- [31] K. Jeong, P. R. Deshmukh, J. Park, Y. Sohn, W. G. Shin, *ACS Sustainable Chem. Eng.* **2018**, *6*, 6518.
- [32] Y. W. Chen, J. D. Prange, S. Dühren, Y. Park, M. Gunji, C. E. D. Chidsey, P. C. McIntyre, *Nat. Mater.* **2011**, *10*, 539.
- [33] K. Kaur, C. V. Singh, *Energy Procedia* **2012**, *29*, 291.
- [34] B. Prasai, B. Cai, M. K. Underwood, J. P. Lewis, D. A. Drabold, *J. Mater. Sci.* **2012**, *47*, 7515.
- [35] S. Selcuk, X. Zhao, A. Selloni, *Nat. Mater.* **2018**, *17*, 923.
- [36] L. Zhang, B. K. Miller, P. A. Crozier, *Nano Lett.* **2013**, *13*, 679.
- [37] L. Shi, Z. Li, T. D. Dao, T. Nagao, Y. Yang, *J. Mater. Chem. A* **2018**, *6*, 12978.
- [38] Z. Guo, F. Ambrosio, A. Pasquarello, *J. Mater. Chem. A* **2018**, *6*, 11804.
- [39] M. Hannula, H. Ali-Löyty, K. Lahtonen, E. Sarlin, J. Saari, M. Valden, *Chem. Mater.* **2018**, *30*, 1199.
- [40] S. Hu, M. R. Shaner, J. A. Beardslee, M. Lichterman, B. S. Brunschwig, N. S. Lewis, *Science* **2014**, *344*, 1005.
- [41] S. Lee, K. Lee, W. D. Kim, S. Lee, D. J. Shin, D. C. Lee, *J. Phys. Chem. C* **2014**, *118*, 23627.
- [42] D. Barreca, G. Carraro, A. Maccato, T. Altantzis, K. Kaunisto, A. Gasparotto, *Cryst. Growth Des.* **2018**, *18*, 2579.
- [43] D. Barreca, G. Carraro, A. Gasparotto, C. Maccato, T. Altantzis, C. Sada, K. Kaunisto, T.-P. Ruoko, S. Bals, *Adv. Mater. Interfaces* **2017**, *4*, 1700161.
- [44] J. F. Moulder, W. F. Stickle, P. E. Sobol, K. D. Bomben, *Handbook of X-Ray Photoelectron Spectroscopy*, Perkin Elmer Corporation, Eden Prairie, MN, USA **1992**.
- [45] Q. Li, X. Sun, K. Lozano, Y. Mao, *J. Phys. Chem. C* **2014**, *118*, 13467.
- [46] Pattern No. 36–1451, JCPDS, **2000**.
- [47] A. Gasparotto, G. Carraro, C. Maccato, C. Sada, J. Balbuena, M. Cruz-Yusta, L. Sánchez, N. Vodišek, U. Lavrenčič Štangar, D. Barreca, *CrystEngComm* **2018**, *20*, 1282.
- [48] J. Shi, *Chem. Rev.* **2013**, *113*, 2139.
- [49] C. Cheng, A. Amini, C. Zhu, Z. Xu, H. Song, N. Wang, *Sci. Rep.* **2015**, *4*, 4181.
- [50] B. Ohtani, Y. Ogawa, S.-i. Nishimoto, *J. Phys. Chem. B* **1997**, *101*, 3746.
- [51] J. Huang, Y. Liu, L. Lu, L. Li, *Res. Chem. Intermed.* **2012**, *38*, 487.
- [52] Y.-K. Hsu, S.-Y. Fu, M.-H. Chen, Y.-C. Chen, Y.-G. Lin, *Electrochim. Acta* **2014**, *120*, 1.
- [53] A. Sreedhar, H. Jung, J. H. Kwon, J. Yi, Y. Sohn, J. S. Gwag, *J. Electroanal. Chem.* **2017**, *804*, 92.
- [54] X. Yang, A. Wolcott, G. Wang, A. Sobo, R. C. Fitzmorris, F. Qian, J. Z. Zhang, Y. Li, *Nano Lett.* **2009**, *9*, 2331.
- [55] A. Sáenz-Trevizo, P. Amézaga-Madrid, P. Pizá-Ruiz, W. Antúnez-Flores, C. Ornelas-Gutiérrez, M. Miki-Yoshida, *Mater. Sci. Semicond. Process.* **2016**, *45*, 57.
- [56] X. Li, C. Wang, N. Xia, M. Jiang, R. Liu, J. Huang, Q. Li, Z. Luo, L. Liu, W. Xu, D. Fang, *J. Mol. Struct.* **2017**, *1148*, 347.
- [57] Y.-C. Huang, S.-Y. Chang, J.-M. Jehng, *J. Phys. Chem. C* **2017**, *121*, 19063.
- [58] D. Barreca, G. Carraro, A. Gasparotto, C. Maccato, C. Sada, E. Bontempi, M. Brisotto, O. Pliekhova, U. Lavrenčič Štangar, *Environ. Sci. Pollut. Res.* **2016**, *23*, 20350.
- [59] P. Schlossmacher, D. O. Klenov, B. Freitag, H. S. von Harrach, *Microsc. Today* **2010**, *18*, 14.